



Shrinking gate fluorescence correlation spectroscopy yields equilibrium constants and separates photophysics from structural dynamics

Tim Schröder^{a,1} , Johann Bohlen^a , Sarah E. Ochmann^a , Patrick Schüler^a , Stefan Krause^{a,2} , Don C. Lamb^a , and Philip Tinnefeld^{a,1}

Edited by Justin R. Caram, University of California Los Angeles, Los Angeles, CA; received July 13, 2022; accepted November 16, 2022 by Editorial Board Member Shaul Mukamel

Fluorescence correlation spectroscopy is a versatile tool for studying fast conformational changes of biomolecules especially when combined with Förster resonance energy transfer (FRET). Despite the many methods available for identifying structural dynamics in FRET experiments, the determination of the forward and backward transition rate constants and thereby also the equilibrium constant is difficult when two intensity levels are involved. Here, we combine intensity correlation analysis with fluorescence lifetime information by including only a subset of photons in the autocorrelation analysis based on their arrival time with respect to the excitation pulse (microtime). By fitting the correlation amplitude as a function of microtime gate, the transition rate constants from two fluorescence-intensity level systems and the corresponding equilibrium constants are obtained. This shrinking-gate fluorescence correlation spectroscopy (sg-FCS) approach is demonstrated using simulations and with a DNA origami-based model system in experiments on immobilized and freely diffusing molecules. We further show that sg-FCS can distinguish photophysics from dynamic intensity changes even if a dark quencher, in this case graphene, is involved. Finally, we unravel the mechanism of a FRET-based membrane charge sensor indicating the broad potential of the method. With sg-FCS, we present an algorithm that does not require prior knowledge and is therefore easily implemented when an autocorrelation analysis is carried out on time-correlated single-photon data.

time-gated fluorescence correlation spectroscopy | autocorrelation analysis | Förster resonance energy transfer | biophysics | DNA origami

Fluorescence correlation spectroscopy (FCS) is a widely used tool to determine physical parameters such as concentration (1–3) and kinetic properties such as diffusion constants (4–7), biomolecular dynamics (8–10), reaction kinetics (11–13) and photophysical processes (14, 15). Time correlation of the fluorescent signal of freely diffusing molecules through a focused laser beam reveals the time scales of the underlying characteristic signal fluctuations. With the aid of physical models, these time scales can be assigned to the different kinetic processes, the most common process being the diffusion of molecules in and out of the laser focus.

Many variants of FCS such as Förster resonance energy transfer-FCS (FRET-FCS) (16, 17), fluorescence lifetime correlation spectroscopy (FLCS) (18, 19), time-gated FCS (20), and single-molecule burst-selective FCS (21, 22) have evolved improving the specificity for underlying processes as well as the deduced information content (23, 24). Beyond diffusion constants and bimolecular binding constants, the fluorescence intensity correlation function $g^{(2)}(\Delta\tau)$ is also a widely employed algorithm to extract kinetic processes within diffusing molecules as well as from immobilized single quantum emitters (25–29). For immobilized molecules, the autocorrelation analysis has been used, for example, to quantify physical and biomolecular processes ranging from antibunching (30, 31) to intersystem crossing (32, 33) and photo-induced electron transfer (34–36) to slower molecular dynamic of DNA hybridization switching (9, 37, 38).

The extraction of kinetic information from binned intensity trajectories acquired from immobilized molecules in single-molecule FRET experiments was recently benchmarked (39). Algorithms based on hidden Markov modeling or line fitting recover kinetic information of the studied system as long as the kinetics is slower than the binning of the intensity trajectory (39). Intensity correlation, on the other hand, can theoretically extract kinetic rate constants from fluctuations faster than the inter-photon time, but it is rarely used to study biological systems. In our lab, we were confronted with the problem that we suspected a correlation component induced by the fluctuating distance of a tethered dye to the quenching surface by graphene energy transfer (GET) (40) in a similar time regime where also photophysical processes (on–off, e.g., triplet transitions) occurred (38).

Significance

Quantification of dynamic information is fundamental to the understanding of many biological processes. However, extraction of quantitative information is often difficult due to mathematical ambiguities or the separation of conformational dynamics from photophysical processes. Here, we present a general approach that analyzes fluorescence intensity fluctuations and fluorescence lifetime information to perform a quantitative analysis of two-state systems without prior knowledge regarding the dynamics. This approach can also distinguish between photophysical on-off processes and dynamic changes between states with different fluorescence lifetime states (e.g., conformational states with different Förster resonance energy transfer (FRET) efficiencies). We demonstrate the power of this method, referred to as shrinking gate (sg)-FCS, by unravelling the mechanism of a FRET-based membrane-charge sensor.

The authors declare no competing interest.

This article is a PNAS Direct Submission. J.R.C. is a guest editor invited by the Editorial Board.

Copyright © 2023 the Author(s). Published by PNAS. This open access article is distributed under [Creative Commons Attribution-NonCommercial-NoDerivatives License 4.0 \(CC BY-NC-ND\)](#).

¹To whom correspondence may be addressed. Email: tim.schroeder@cup.uni-muenchen.de or philip.tinnefeld@cup.uni-muenchen.de.

²Present address: Fraunhofer Institut für Integrierte Schaltungen IIS, 01187 Dresden, Germany.

This article contains supporting information online at <https://www.pnas.org/lookup/suppl/doi:10.1073/pnas.2211896120/-/DCSupplemental>.

Published January 18, 2023.

The problem to separate both contributions arose and we realized that this problem was not sufficiently addressed by other approaches including FLCS and FRET-FCS. FLCS, for example, extracts separate correlation functions when mixtures of species are involved but requires prior knowledge of the fluorescence lifetimes of the species involved (18, 19). FRET-FCS separates biomolecular dynamics from on-off processes but is underdetermined for extracting equilibrium constants. Furthermore, it requires fluorescent acceptors (16).

On-off switching by photophysical processes and distance-dependent quenching by, for example, GET or by a FRET acceptor both induce intensity fluctuations that appear as a correlation in the intensity correlation function $g^{(2)}(\Delta\tau)$. The two processes differ in that only the dynamic quenching processes induce a change of the fluorescence lifetime. Thus, we reasoned that it required an algorithm to correlate the fluorescence lifetime information with the amplitude of the correlation function without prior assumptions. These considerations motivated us to revisit the influence of time-gating on the bunching amplitudes in FCS and for the correlation analysis in general.

In this paper, we present a simple and versatile method to connect the fluorescence lifetime with the autocorrelation information, termed shrinking-gate FCS (sg-FCS), which enables the separation of dynamic quenching processes from on-off processes. By acquiring time-correlated single photon counting data, we have, on the one hand, the information on the number of laser pulses emitted since the beginning of the experiment until the photon was detected, which is commonly referred to as macrotime. This information is used to calculate the binned intensity trajectory and the intensity correlation function. On the other hand, we record the time between laser pulse and photon detection, which is commonly referred to as the microtime. The microtime contains the information regarding the excited state lifetime. In sg-FCS, we calculate the fluorescence intensity correlation function using different subsets of photons depending on their time lag with respect to the laser pulse (i.e., their microtime). Plotting the correlation amplitude as a function of the microtime threshold shows how the correlation amplitude is increasingly dominated by the long-lifetime component. We present a model for this dependence based on a two-state system that yields further important parameters such as transition times and the equilibrium constant that are not directly obtainable from ordinary autocorrelation functions. The analysis can be carried out without prior knowledge of fluorescence lifetimes and it directly reveals whether the correlation amplitudes are of photophysical (on-off) origin or whether states of different fluorescence lifetimes are involved. Using simulations and DNA origami-pointer model systems, we show that the algorithm works even when the dwell times in the individual states are unbalanced ($K \ll 1$ or $K \gg 1$). We exemplify the strength of this approach using graphene quenching as well as in single-molecule FRET experiments of a novel membrane surface potential sensor. The method is robust within the defined limits and easy to implement suggesting that it should be considered whenever FCS and related autocorrelation analyses are combined with time-correlated single-photon counting (TCSPC) information.

Results

Intensity fluctuations on different time scales, e.g., caused by diffusion, photophysics (pp) or distance changes of a FRET pair, are commonly analyzed with the normalized second-order intensity correlation given by:

$$g^{(2)}(\Delta\tau) = \frac{\langle I(t) \cdot I(t + \Delta\tau) \rangle}{\langle I(t) \rangle^2}, \quad [1]$$

which correlates the measured intensity $I(t)$ with the measured intensity as a function of the lag time, $\Delta\tau$.

A process that undergoes stochastic switching between a fluorescent state A and a non-fluorescent state B results in a monoexponential decay component of the $g^{(2)}(\Delta\tau)$ function (15).



Here, k_A and k_B represent the transition rate constant into state A or state B , respectively. For diffusing molecules, the relaxation kinetics is superimposed with the diffusion correlation function according to the following equation of $g^{(2)}(\Delta\tau)$.

$$g^{(2)}(\Delta\tau) = \frac{\gamma_{FCS}}{N} \cdot \frac{1}{1 + \frac{\Delta\tau}{\tau_{diff}}} \cdot \frac{1}{\sqrt{1 + \frac{\Delta\tau}{w^2 \cdot \tau_{diff}}}} \cdot \left(1 + A_{dyn} \cdot e^{-\frac{\Delta\tau}{\tau_{CRT}}} \right) + 1. \quad [3]$$

Here, γ_{FCS} accounts for the approximated Gaussian illumination profile and corresponds to $2^{-\frac{3}{2}}$, N denotes the average number of molecules in the detection volume, τ_{diff} the diffusion dwell time and w accounts for the different axial dimension of the three-dimensional confocal volume ($w = \frac{w_z}{w_{xy}}$). The dynamic bunching amplitude A_{dyn} accounts for the photon bunching due to fast fluorescence intensity fluctuations on short time scales and is equal to the equilibrium constant in the case of on-off switching with the correlation relaxation time (CRT) τ_{CRT} .

To simplify the discussion, we first consider immobilized molecules undergoing fluctuations between different intensity states. However, we note that sg-FCS is applicable whenever there are two components with different fluorescence lifetimes that exchange due to various quenching mechanisms. With the fitted CRT and bunching amplitude, the dwell times for each state can be calculated according to $\tau_{CRT} = \frac{1}{k_A + k_B}$ and $A_{dyn} = \frac{k_B}{k_A}$ also yielding the equilibrium constant K . When dynamic quenching with nonzero intensity states are involved such as in FRET experiments, the calculation of the donor bunching amplitude A_{dyn} is “convoluted” with the intensity contrast of the two FRET states (17, 20, 41, 42).

$$A_{dyn} = K \left(\frac{I_A - I_B}{I_A + K \cdot I_B} \right)^2, \quad [4]$$

where I_A and I_B represent the fluorescence intensity of state A (high-intensity, long fluorescence lifetime state) and state B (low-intensity, short fluorescence lifetime state). K denotes the equilibrium constant as the ratio of the switching rate constants between the high- and low-intensity states $K = \frac{k_B}{k_A}$. As Eq. 4 shows, the donor bunching amplitude A_{dyn} for a two intensity-state model relies on the fractional intensity difference. Due to the quadratic intensity difference dependence of the intensity correlation function, no unique solution for K is obtained even when both intensity levels are known (which is commonly not the case or there is some uncertainty involved). We demonstrate this by simulating two intensity trajectories of immobilized molecules, which are shown in Fig. 1A (see *SI Appendix, section 1* for detailed information on the simulations). Both intensity trajectories have the same intensities for the high- and low-intensity states,

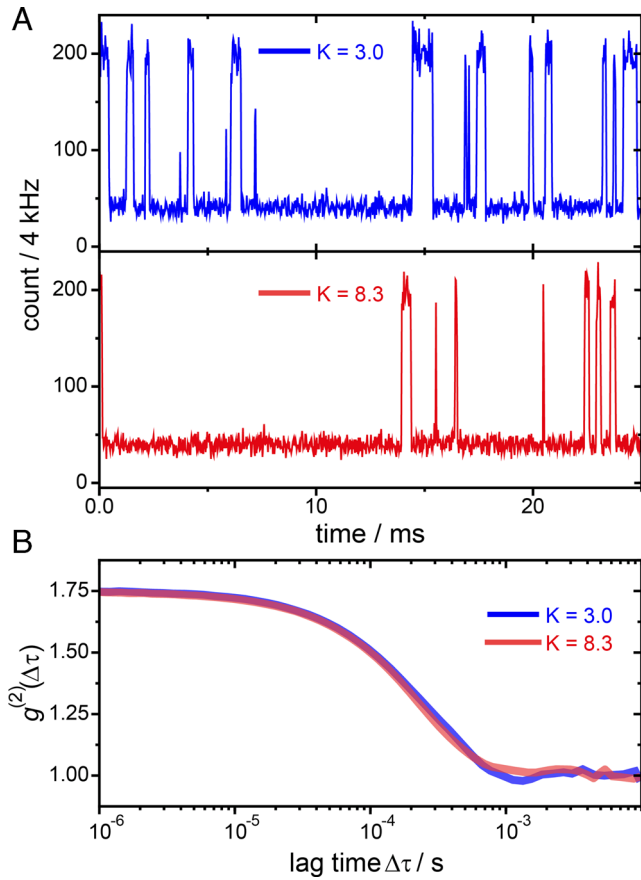


Fig. 1. The ambiguity of the intensity autocorrelation function. (A) A short section of the simulated intensity trajectories where the respective intensity levels for the bright and quenched states are the same but with different equilibrium constants, K . The rate constants for switching in the blue and red trajectories are given in Table 1. (B) The autocorrelation of the full simulated trajectories, portions of which are shown in a).

respectively. It is obvious from the trajectories that the switching kinetics are different and that the red trajectory shows a longer dwell time in the fluorescence-quenched state.

Despite the different equilibrium constants, K , of the trajectories in Fig. 1A, the autocorrelations in Fig. 1B are virtually identical. They have the same bunching amplitude $A_{dyn}(t_g)$ and CRT τ_{CRT} . With a single $g^{(2)}(\Delta\tau)$ correlation, it is impossible to extract the switching rate constants and describe the kinetics quantitatively. This important information is, however, accessible by connecting the autocorrelation with the fluorescence lifetime information. We do this using sg-FCS, where subsets of photons are correlated depending on the arrival time of the photon with respect to the laser pulse (the microtime). By varying the threshold for the microtime, the relative intensity of the two states are changed and thereby their influence on the amplitude of the intensity correlation function. Hence, the intensity correlation function becomes a function of delay, $\Delta\tau$, and microtime gate, t_g : $g^{(2)}(\Delta\tau, t_g)$. The effect of the microtime thresholding on the fluorescence intensity trajectory and on the autocorrelation function is depicted in Fig. 2A–C using the simulated data from Fig. 1, Fig. 2A shows the biexponential fluorescence lifetime histogram of the simulated data with $\tau_A = 4.0$ ns and $\tau_B = 0.8$ ns. The shaded area indicates the subset of photons selected for different microtime gates. Fig. 2B shows the corresponding intensity time

traces and Fig. 2C shows the corresponding $g^{(2)}(\Delta\tau, t_g)$ correlation.

When considering all photons in this simulation, i.e., when the microtime threshold is set to $t_g = 0$ ns, the fluorescence intensity trajectory and autocorrelation function are the same as the ones shown in Fig. 1A (blue trajectory). When only photons after $t_g = 1.5$ ns are considered, the intensity of the fluorescence intensity trajectory is reduced. The intensities of the two fluorescent states, however, are not affected equally. The microtime gate preferentially excludes photons from the quenched intensity state I_B because it has the shorter fluorescence lifetime. The result is a higher intensity contrast between the two states, which results in a higher bunching amplitude $A_{dyn}(t_g)$ of the autocorrelation in accordance with Eq. 4. For a higher microtime threshold of $t_g = 6$ ns after laser excitation, almost no photons from the quenched state remain and the trajectory is dominated by bursts of photons from the bright fluorescent state. With the microtime gating, the situation has changed from a “high-intensity” – “low-intensity” fluorescent trajectory to an “on” – “off” trajectory similar to photophysical blinking. Therefore, the bunching amplitude $A_{dyn}(t_g)$ is maximized and represents the equilibrium constant K .

Applying shrinking-gate FCS with a stepwise increase of the gating threshold to the trajectories of Fig. 1A now yields distinguishable correlation functions (Fig. 2D). When considering all photons, the bunching amplitude $A_{dyn}(t_g = 0$ ns) is the smallest and is identical for the two trajectories. By applying sg-FCS from $t_g = 0.0$ ns to $t_g = 8.0$ ns with a step size of 0.5 ns, the amplitudes increase differently and saturate at the respective equilibrium constants that were fed into the simulation.

Each sg-FCS curve is fitted by a monoexponential model yielding the bunching amplitude $A_{dyn}(t_g)$.

$$g^{(2)}(\Delta\tau, t_g) = 1 + A_{dyn}(t_g) \cdot e^{-\left(\frac{\Delta\tau}{\tau_{CRT}}\right)}, \quad [5]$$

The extracted bunching amplitudes, $A_{dyn}(t_g)$, are plotted as a function of the microtime threshold t_g in Fig. 2E. To fit the data, we first consider how the intensity of each state is changing depending on the microtime gate t_g . We assume that both intensity states decay with their characteristic fluorescence lifetime, which is inversely proportional to the excited state decay rate constant.

$$I_A(t_g) = I_0 \int_{t_g}^{\infty} e^{-(k_r + k_{nr}) \cdot t'} dt' = \frac{e^{-(k_r + k_{nr}) \cdot t_g}}{(k_r + k_{nr})}, \quad [6]$$

$$I_B(t_g) = I_0 \int_{t_g}^{\infty} e^{-(k_r + k_{nr} + k_{\Delta ET}) \cdot t'} dt' = \frac{e^{-(k_r + k_{nr} + k_{\Delta ET}) \cdot t_g}}{(k_r + k_{nr} + k_{\Delta ET})}. \quad [7]$$

Here, k_r denotes the radiative rate constant and k_{nr} all non-radiative decay rate constants of the low FRET state, I_A , which includes possible energy transfer to an acceptor dye. $k_{\Delta ET} = k_{ET, high FRET} - k_{ET, low FRET}$ denotes the additional energy transfer rate constant of the high FRET state, I_B . I_0 is a scaling factor. Considering the different fluorescent decays for

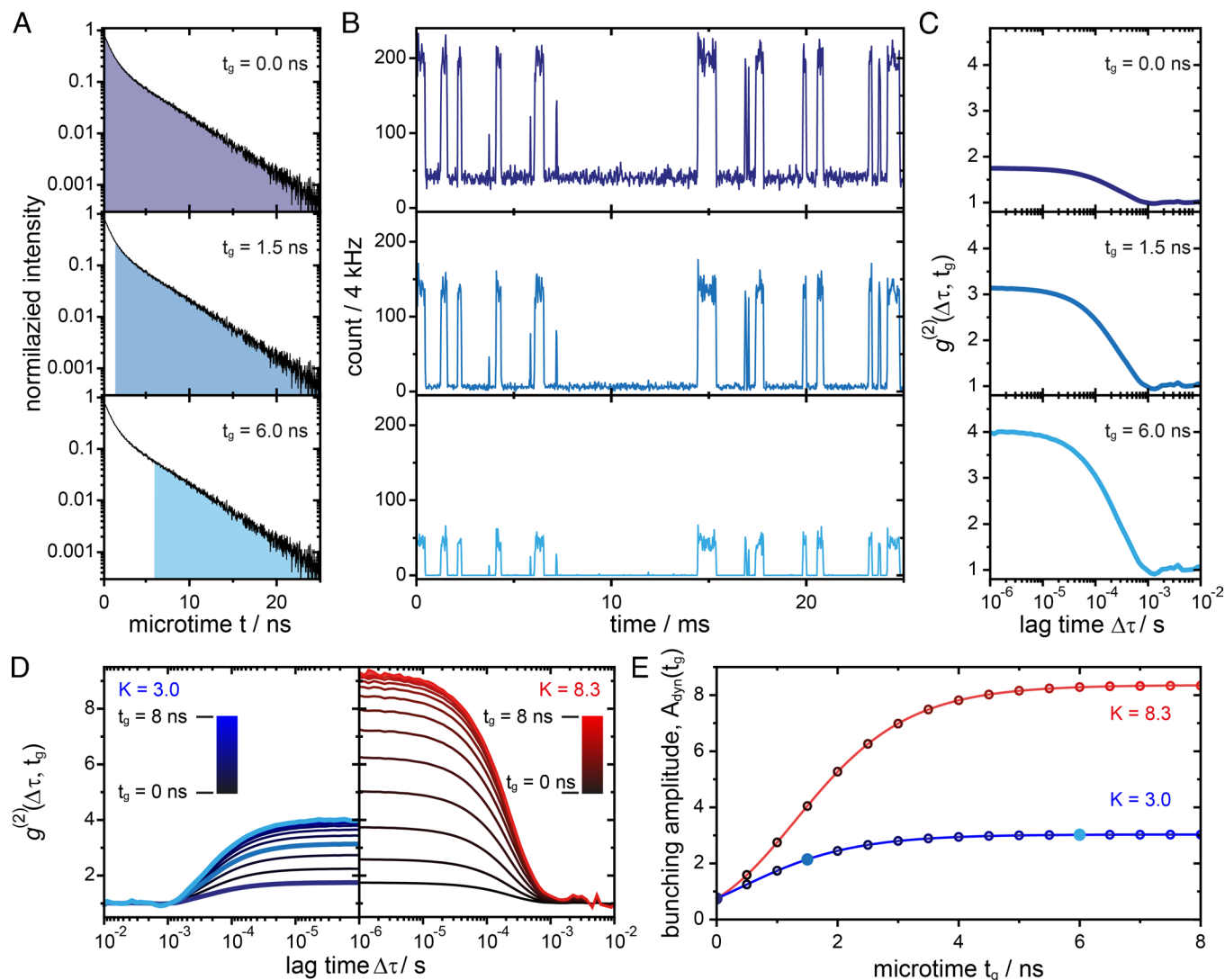


Fig. 2. Applying sg-FCS to the simulated data from Fig. 1. (A) Histograms of simulated photon arrival times in a pulsed-laser excitation experiment. The shaded area indicates the applied microtime gate for sg-FCS. (B) Extracted intensity trajectories according to the selected photons from the fluorescence lifetime data. (C) The corresponding $g^{(2)}(\Delta\tau, t_g)$ of the respective intensity trajectories. (D) The autocorrelation function is plotted as a function of the shrinking-gate in sg-FCSs for the simulated intensity trajectories of Fig. 1A. The sg-FCS correlation functions are indicated with a color gradient from black $g^{(2)}(\Delta\tau, t_g = 0 \text{ ns})$ to blue (Left, $K = 3$) or red (Right, $K = 8.3$) $g^{(2)}(\Delta\tau, t_g = 8 \text{ ns})$ with a 0.5 ns step size. Correlations shown in C are highlighted in the corresponding bold blue color. The $g^{(2)}(\Delta\tau, t_g)$ correlation functions are fitted with a monoexponential model and the obtained correlation amplitudes $A_{dyn}(t_g)$ are plotted in E. The data points are fitted with the model of Eq. 9 to extract the equilibrium constant K and $k_{\Delta ET}$. The full circles represent the amplitude of the correlation functions in colors corresponding to panels C and D.

both intensities in Eq. 4, we obtain the microtime threshold-dependent bunching amplitude $A_{dyn}(t_g)$:

$$A_{dyn}(t_g) = K \left(\frac{1 - \frac{k_r + k_{nr}}{k_r + k_{nr} + k_{ET}} e^{-k_{\Delta ET} \cdot t_g}}{1 + K \cdot \frac{k_r + k_{nr}}{k_r + k_{nr} + k_{ET}} e^{-k_{\Delta ET} \cdot t_g}} \right)^2. \quad [8]$$

Eq. 8 enables us to extract two parameters from sg-FCS. First of all, the exponential term describes the rising intensity contrast between the intensity states with respect to the beginning of the microtime gate, which allows the recovery of $k_{\Delta ET}$. Secondly, at high-intensity contrast, the bunching amplitude $A_{dyn}(t_g)$ saturates at the value of the equilibrium constant K . Eq. 8 is determined assuming that the excitation pulse is a delta function at $t_g = 0 \text{ ns}$. In a real experiment, the arrival of the laser pulse is

not exactly synchronized to the start of the TAC bins. Hence, we also have to include an offset of the electronics with respect to the arrival of the laser pulse, t_{shift} .

$$A_{dyn}(t_g) = K \left(\frac{1 - e^{-k_{\Delta ET}(t_g - t_{shift})}}{1 + K \cdot e^{-k_{\Delta ET}(t_g - t_{shift})}} \right)^2. \quad [9]$$

t_{shift} aggravates fitting and extraction of the parameters of interest (see *SI Appendix, sections 2 and 3* for a detailed discussion of the fitting model). With Eq. 9, we can fit the bunching amplitudes $A(t_g)$ in Fig. 2E and extract the equilibrium constants, K , and the additional energy transfer rate constant of the high FRET state, $k_{\Delta ET}$ (Table 1). Both functions in Fig. 2E start with an initial intensity contrast of $\frac{I_A}{I_B} = \frac{\tau_A}{\tau_B} = 5$ with fluorescence lifetimes of $\tau_A = 4 \text{ ns}$ and $\tau_B = 0.8 \text{ ns}$, respectively. The function saturates

Table 1. The sg-FCS recovered rate constants from a least square fit to the data in Fig. 2E along with the corresponding errors given in the fit parameters

	Simulation	Fit	Simulation	Fit
$K / 1$	3	3.031 ± 0.001	8.33	8.352 ± 0.003
k_A / s^{-1}	1,000	960 ± 10	428.5	432 ± 5
k_B / s^{-1}	3,000	$2,900 \pm 30$	3,571.4	$3,570 \pm 40$
$k_{\Delta ET} / ns^{-1}$	1	1.001 ± 0.001	1	1.002 ± 0.001

around a microtime threshold of $t_g = 6$ ns. At this point, the long component contributes by a factor of $\frac{I_A(t_g = 6 \text{ ns})}{I_B(t_g = 6 \text{ ns})} = e^{k_{\Delta ET} t_g} \sim 400$ more (for $k_{\Delta ET} = 1 \text{ ns}^{-1}$) to the autocorrelation function than the short component. The two graphs saturate at the two different amplitudes representing the different equilibrium constants.

When changing from simulations to real data analysis, we have to consider uncorrelated background, e.g., from detector dark counts and/or luminescence from the immersion oil. Uncorrelated background leads to a decrease in the correlation amplitude (43, 44). As the fluorescence signal decays after pulsed laser excitation, the signal-to-background ratio decreases for long microtime gates t_g resulting in a decaying bunching amplitude $A_{dyn}(t_g)$. To extract the correct equilibrium constant K , each bunching amplitude has to be background-corrected, which we describe in detail in the supporting information *SI Appendix, section 4* when dealing with experimental data.

For sg-FCS, the fluorescence lifetime information is used and hence pulsed laser excitation is required. We use an amplified picosecond pulsed laser to excite the donor dye at 532 nm. The laser is focused on the sample by an objective, which also collects the fluorescence of a single structure of interest. The fluorescence signal is split into the donor and acceptor fluorescence signal by a dichroic beamsplitter. A single-pixel single-photon-counting module in each channel detects the fluorescence and a TCSPC module correlates the detection events with respect to the last laser pulse and the beginning of the experiment. For more details of the confocal setup see *SI Appendix, section 11 and Materials and Methods*.

To test sg-FCS with real data, we used a two-state molecular model system with well-controllable transition rate constants. A Cy3B-labeled pointer DNA strand is tethered to an L-shaped DNA origami (38, 45, 46) structure and transiently binds to two protruding strands as depicted in Fig. 3A. Next to the lower binding site, an acceptor dye, ATTO647N, is placed so that a high FRET signal is observed when the pointer strand binds to the complementary staple strand placed near the acceptor dye. Hence, switching between a low-FRET state and a high-FRET state is observed and the kinetics can be tuned by the number of bases and the sequence of the complementary strand (for sequence information, see *SI Appendix, section 5*). For example, 7-nt complementary bases correspond to binding times on the millisecond to second timescale (38, 46). The DNA origami structures were immobilized on a BSA-biotin NeutrAvidin passivated glass slide and fluorescence intensity trajectories from single structures were acquired with a confocal microscope. A representative fluorescence intensity trajectory of the donor dye (blue) and the corresponding sensitized acceptor signal (orange) is shown in Fig. 3B. The donor and acceptor signal exhibit anticorrelated behavior due to the switching of the protruding pointer strand between the two binding positions.

For the sg-FCS analysis, we first calculate the $g^{(2)}(\Delta\tau)$ autocorrelation function including all photons ($g^{(2)}(\Delta\tau, t_g = 0 \text{ ns})$) (Fig. 3C) to extract the CRT, τ_{CRT} . In this case, $\tau_{CRT} = 0.67 \pm 0.02$ s. Next, sg-FCS is applied with a step size of 0.2 ns and the background corrected bunching amplitudes $A_{dyn}(t_g)$ (see *SI Appendix, section 4* for details) are extracted from a monoexponential fit (Eq. 4) to the autocorrelation function. The bunching amplitudes $A_{dyn}(t_g)$ are plotted in Fig. 3D where the error bars correspond to the fit error of the bunching amplitude term $A_{dyn}(t_g)$. The first data points do not show a change in the bunching amplitude $A_{dyn}(t_g)$ because the laser pulse arrives at ~ 1 ns. Therefore, only data points arriving after 1.2 ns are considered for the fitting, yielding $k_{\Delta ET} = 0.811 \pm 0.008 \text{ ns}^{-1}$ and an equilibrium constant of $K = 0.547 \pm 0.001$. The extracted additional energy transfer rate constant of the sg-FCS approach matches the value extracted from the lifetime trace of $k_{\Delta ET}^{lifetime} = 0.8 \pm 0.2 \text{ ns}^{-1}$ (*SI Appendix, Fig. S6 and section 6*). With τ_{CRT} and K , we calculate the dwell times as $t_{sg-FCS, low FRET} = 1.90 \pm 0.06$ s and $t_{sg-FCS, high FRET} = 1.04 \pm 0.04$ s. We compared our sg-FCS results with a hidden Markov model (HMM) analysis, which is used to analyze real-time trajectories of slow transitions such as those observed for Holliday Junction-kinetics (47, 48). A HMM trajectory of an example trajectory is plotted as black line on top of the donor signal in Fig. 3B and the extracted dwell times are $t_{HMM, low FRET} = 2.1 \pm 0.3$ s and $t_{HMM, high FRET} = 1.2 \pm 0.2$ s. This is in good agreement with the sg-FCS results. The dwell times of the high- and low-FRET state for several molecules are registered in a scatter plot in Fig. 3E for the 7-nt sample (black dots). Interestingly, the median from 67 trajectories yields $K = 0.55$, i.e., < 1 although both FRET positions have equal complementary sequences. This is a real difference in the kinetic rates, which we attribute to details of the DNA origami itself (*SI Appendix, section 6*).

To explore the dynamic range of kinetics that can be assessed by sg-FCS, we vary the protruding binding sites of the DNA origami structure and measure different combinations of complementary sequences (see *SI Appendix, section 5* for sequence information). By removing one G-C stacking interaction, for example, the switching kinetics become ~ 50 -fold faster and a loss of A-T stacking by introducing an A-C mismatch accelerates the kinetics ~ 5 -fold (Fig. 3E). With 5-nt complementary bases, the binding times are shifted into the hundred- μ s regime and cannot be extracted using an HMM analysis.

When the difference between the transition rates becomes too drastic, the signature of the short-lived state gets lost in the statistical correlation analysis. Nevertheless, sg-FCS is still able to extract a $K \sim 0.01$ for the 6- \leftrightarrow 7-nt binding construct (see the purple data points in Fig. 3E). This indicates a hundred times longer dwell time in the low FRET state compared to the high FRET state. Although the correlation amplitudes $A_{dyn}(t_g)$ are small, they are precise due to the high count rate in our experiment leading to a sufficient signal-to-noise ratio (*SI Appendix, section 7*). The upper limit for our system is an equilibrium constant of $K \sim 8$ (see green data points in Fig. 3E), which corresponds to longer dwell times in the high-FRET state leading to less signal in the donor detection channel. Hence, the statistics suffer from low intensities at long thresholds. For shorter gates, the low signal-to-background ratio also limits the analysis (*SI Appendix, section 7*). Interestingly, HMM is able to extract the designed switching kinetics exemplifying its potential to analyze rare events in the regime of slow kinetics (*SI Appendix, Fig. S5*).

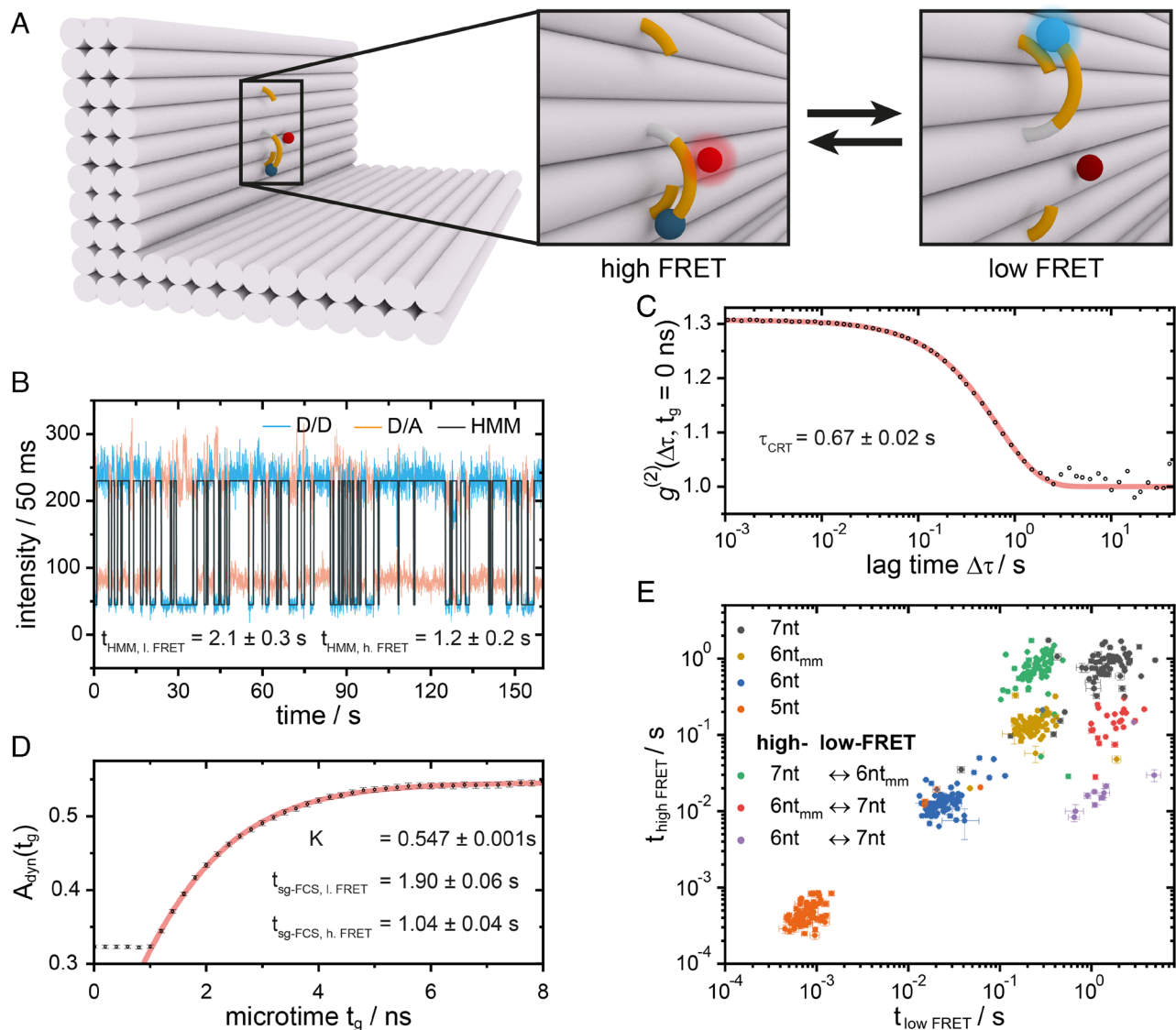


Fig. 3. sg-FCS applied to analyze the dynamics of a DNA origami. (A) Sketch of the L-shaped DNA origami structure. The zoom-ins show the low-FRET (*Top*) and high-FRET (*Bottom*) binding conformations of the blue donor dye (Cy3B). The red acceptor dye (ATTO647N) position is fixed on the DNA origami structure. (B) A typical single particle fluorescence intensity trajectory with 7-nt complementary bases shows the donor intensity (D/D) in blue and the acceptor intensity after donor excitation (D/A) in orange. The black line indicates the most likely FRET trajectory generated by a hidden Markov model analysis. (C) The $g^{(2)}(\Delta\tau, t_g = 0 \text{ ns})$ correlation function of the donor fluorescence intensity trajectory (D/D) (black dots) with a monoexponential fit Eq. 4, red transparent line. (D) Background corrected amplitudes $A_{\text{dyn}}(t_g)$ from the sg-FCS analysis (black dots) fitted using Eq. 9 (red transparent line). (E) A scatterplot of the average binding times in the low- and high-FRET positions acquired from the sg-FCS analysis for a multitude of constructs given in the panel legend. The binding kinetics was tuned by the number of complementary bases. Only trajectories with at least ten transitions between different fluorescence intensity states were analyzed. The complementary bases for the high FRET and low FRET conformations were the same unless indicated otherwise. mm: mismatch.

We have demonstrated the effectiveness of the sg-FCS analysis on an immobilized model system. However, it can also be applied to diffusing molecules provided that the kinetics are faster than the diffusion time. Here, we compare the slow-kinetic 7-nt sample with the 5-nt sample. The average diffusion time through the confocal volume is $\tau_{\text{diff}} \sim 1.2 \text{ ms}$ for the DNA origami structure (see *SI Appendix, section 8* for details). In the surface experiments, the CRT τ_{CRT} of the 7-nt sample is on the 600 – 700 ms time scale, i.e., much slower than the diffusion time, whereas it is faster than the diffusion time ($\tau_{\text{CRT}} = 0.3 \text{ ms}$) for the 5-nt sample. Carrying out a single-molecule burst analysis at diluted concentration yields two FRET-populations for the 7-nt sample and one population for the 5-nt sample as the fast kinetics of the 5-nt sample yield an averaged FRET-value during the focal transit (see *SI Appendix, section 8* for solution-based pulsed-interleaved excitation FRET experiments and analysis).

Fig. 4A shows sg-FCS of the 7-nt sample normalized with respect to the diffusion amplitude $G(0)$. A small bunching amplitude $A_{pp,7nt}(t_g)$ at $\tau_{pp} = 46 \mu\text{s}$ is visible but does not change when the gate is varied indicating an on-off process, i.e., pp. The 5-nt sample, on the other hand, shows an additional bunching amplitude $A_{dyn,5nt}(t_g)$ at $\tau_{dyn} = 220 \mu\text{s}$, which varies with the shrinking gate indicative of the expected dynamics (see Fig. 4B and *SI Appendix, section 8* and Table S2 for fit results). The variation of the bunching amplitude $A_{dyn,5nt}(t_g)$ is illustrated by a color gradient from short (black) to late (blue and red, respectively) microtime thresholds in Fig. 4A and B. The extracted kinetics (see *SI Appendix, section 8* for sg-FCS fit) of $t_{l,\text{FRET}} = 330 \pm 30 \mu\text{s}$ and $t_{h,\text{FRET}} = 700 \pm 70 \mu\text{s}$ agree well with the mean kinetics measured on the surface

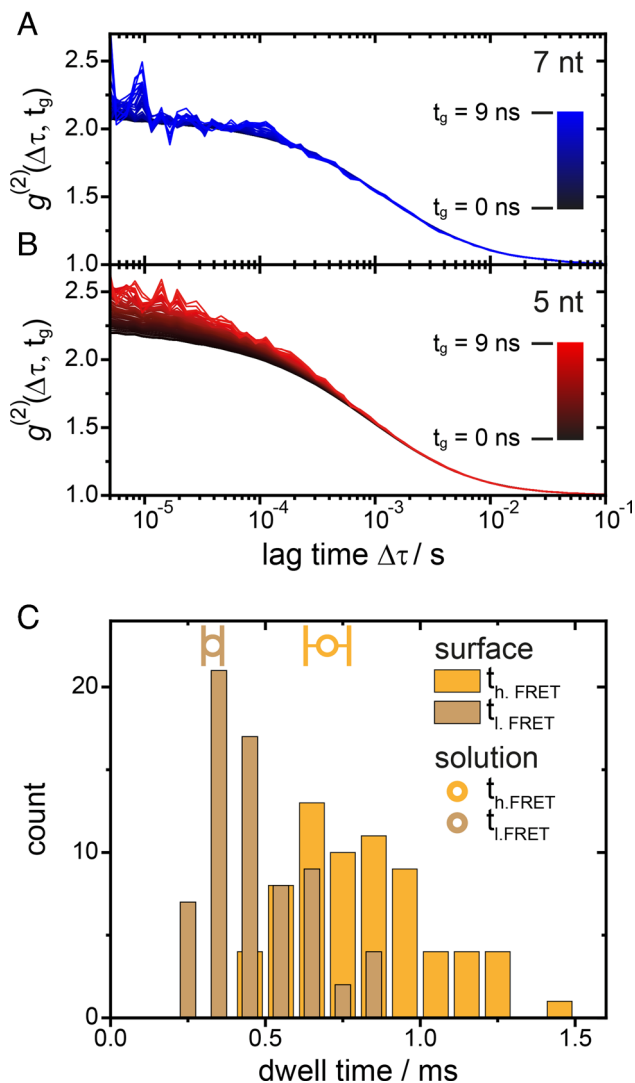


Fig. 4. Solution-based sg-FCS. (A) Diffusion normalized sg-FCS curves of the 7-nt DNA origami structure, which exhibits slower switching kinetics than the diffusion time in the focal volume. No change in bunching amplitude $A_{pp,7nt}(t_g)$ is observed. sg-FCS correlations are indicated with a color gradient from black $g^{(2)}(\Delta\tau, t_g = 0 \text{ ns})$ to blue $g^{(2)}(\Delta\tau, t_g = 9 \text{ ns})$ with a 0.2 ns step size. (B) Diffusion normalized sg-FCS curves of the 5-nt DNA origami structure, which has switching kinetics that is faster than the diffusion time in the focal volume leading to a change of the dynamic bunching amplitude $A_{dyn,5nt}(t_g)$ indicated by the color gradient from black $g^{(2)}(\Delta\tau, t_g = 0 \text{ ns})$ to red $g^{(2)}(\Delta\tau, t_g = 9 \text{ ns})$ with a 0.2 ns step size. (C) Histogram of the sg-FCS kinetics of the 5-nt DNA origami structure from surface experiments. The high-FRET dwell times (orange) and low-FRET dwell times (light brown) match the sg-FCS values from solution experiments, which are indicated above the histogram as circles with error bars representing the SEs.

$t_{l,FRET} = 410 \pm 10 \mu\text{s}$ and $t_{h,FRET} = 770 \pm 20 \mu\text{s}$ with a slight shift towards faster switching kinetics (Fig. 4C), which may be due to the challenges of extracting both the relaxation time and diffusion time from the fit to the autocorrelation function.

The application of sg-FCS is not limited to FCS experiments involving FRET, but proves to be very helpful in experiments where pp and dynamics appear simultaneously. FRET-FCS gives an anticorrelation for dynamic processes but this approach is only applicable when a fluorescent acceptor dye is present in the experiment. In addition, negative bunching amplitudes of FRET-FCS are reduced by the influence of direct excitation of the acceptor and bleed-through from the donor into the acceptor channel (16). When a dark quencher is involved, we cannot simply assign the

bunching amplitude to dynamics or pp using an ordinary $g^{(2)}(\Delta\tau)$ correlation function.

sg-FCS enables this assignment directly and without a change in the experiment's parameters, when the pp results in total quenching and not in a second, low-intensity fluorescence state. In this case, the intensity of the off-state does not change with the microtime gate. We demonstrate this using the same L-shaped DNA origami structure placed on top of a monolayer of graphene (Fig. 5A). A Cy3B labeled DNA tether of 44-nt-long double-stranded DNA (dsDNA) is attached to the DNA origami structure by a 6-nt-long single-stranded DNA (ssDNA) such that it can undergo confined Brownian motion. In this experiment, graphene acts as a two-dimensional energy transfer acceptor resulting in an energy transfer distance dependency of r^{-4} with a broadband quenching efficiency of 50% at a distance of $\sim 18 \text{ nm}$ (40). The closer the dye gets to the graphene, the lower its quantum yield and the shorter its fluorescence lifetime. The DNA origami structure has two layers of dsDNA between graphene and the tether to avoid sticking of the dye to graphene.

The exemplary fluorescence intensity trajectory in Fig. 5B shows dark states on the seconds time scale that most likely originate from radical ion states (34). The autocorrelation function (Fig. 5C) reveals an additional component at $10 \mu\text{s}$ that is not easily assigned to pp or to the molecular dynamics of the tether movement in the graphene quenching field. However, as the amplitude of this component clearly increases with the sg-FCS threshold (Fig. 5D), it is unequivocally ascribed to a process that is associated with a change in fluorescence lifetime, i.e., the Brownian motion of the tether and the subsequent GET quenching. The pp component at 1 s, on the other hand, is clearly not affected by the applied microtime gate. In the example shown in Fig. 5B, the time scales of the bunching components are well separated. However, photophysical and dynamic processes can still be distinguished even if they occur on similar time scales by using the appropriate subsets of photons for the fluorescence intensity correlation analyses (see *SI Appendix, section 9* for details).

The graphene example demonstrates the ability of sg-FCS to distinguish photophysical on-off switching from energy transfer changes in combination with a dark acceptor. In the next example, we use sg-FCS to simultaneously determine the equilibrium coefficients and changing FRET efficiencies in a novel FRET sensor (49) designed for measuring membrane surface charges. The membrane surface charges of cells and changes thereof are involved in various cell signaling pathways (50, 51). Our sensor design (Fig. 6A) is based on a rectangular DNA origami structure equipped with cholesterol moieties for binding to lipid membranes and with biotin for surface immobilization (49). A FRET-based sensing unit is placed on the DNA origami structure consisting of the anionic donor dye ATTO542 on a flexible ssDNA leash and the acceptor dye ATTO647N, which localizes in the hydrophobic core of the membrane. The anionic sensing unit is expected to adapt its conformation depending on the charge of the membrane surface. This conformational adaptation is monitored by changes in the FRET signal. We studied the mechanism of the charge sensor on large unilamellar vesicles (LUVs) with different compositions of the zwitterionic lipid DOPC (1,2-dioleoyl-sn-glycero-3-phosphocholine) and the anionic lipid DOPG (1,2-dioleoyl-sn-glycero-3-phospho-(1'-rac-glycerol)) yielding a series of LUVs with different surface charges.

Using a total internal reflection wide-field setup with continuous wave laser excitation, different uncorrected FRET-efficiencies ($E_{0DOPG} \sim 0.52$ and $E_{80DOPG} \sim 0.42$) were measured for the sensor exposed to LUVs containing 0% and 80% of the anionic lipid

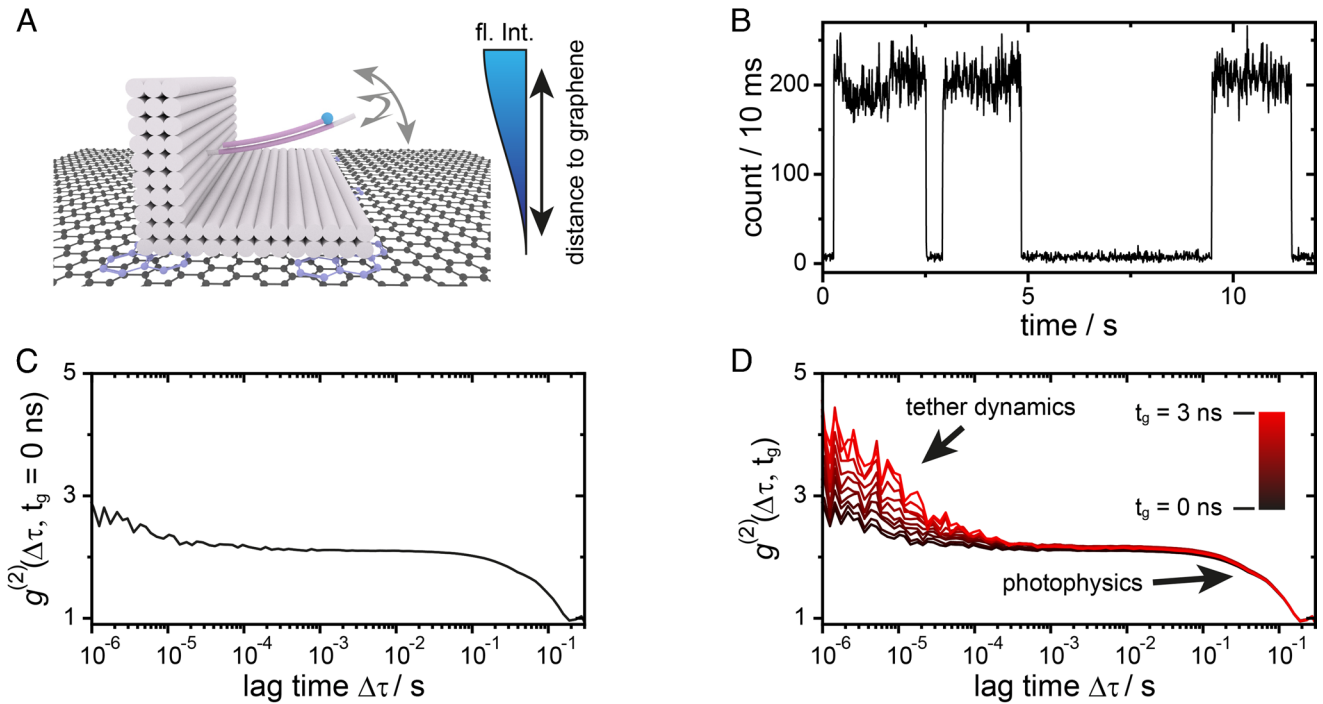


Fig. 5. sg-FCS applied to a dynamically quenching system. (A) Sketch of the L-shaped DNA origami structure on a single layer of graphene which acts as 2D FRET quencher. At the tip of the tether, a Cy3B dye (blue dot) is attached, which changes its fluorescence intensity and fluorescence lifetime on the μs timescale due to Brownian fluctuations in the distance between the dye and graphene. Pyrene molecules (in purple) were attached to the DNA origami to better align the DNA origami on the graphene (40). (B) A single-molecule fluorescence trajectory from a DNA origami on graphene showing variations in fluorescence intensity due to distance fluctuations as well as off states [most likely due to radical ion states (35)] on the second timescale. (C) FCS intensity correlation analysis of the fluorescence trajectory in (B). What gives rise to the fast-bunching amplitude is not clear from a single autocorrelation function. (D) sg-FCS analysis of the fluorescence trajectory in (B). The beginning of the microtime gate is indicated by the color gradient from black $g^{(2)}(\Delta\tau, t_g = 0 \text{ ns})$ to red $g^{(2)}(\Delta\tau, t_g = 3 \text{ ns})$ with a 0.2 ns step size. From the gate dependence of the correlation amplitude, we can attribute the fast bunching term to diffusion of the tether with respect to the graphene surface.

DOPG (49). Intuitively, the decreased FRET signal suggests further separation of the two dyes when the DOPG content is higher. The question arises whether the Coulomb repulsion simply induces a higher average distance of the flexible signaling unit or the system is more complex. Thus, we investigated our DNA origami surface charge sensor on a TCSPC confocal microscope with pulsed laser excitation and higher time resolution by placing one molecule at a time in the laser focus. The $g^{(2)}(\Delta\tau)$ intensity correlation function of an exemplary donor intensity trajectory reveals a mono-exponential photon bunching behavior for both lipid compositions (Fig. 6B). The 0% DOPG sample (blue) shows a faster CRT of $\tau_{0\% \text{ DOPG}} = 0.45 \pm 0.01 \text{ ms}$. With the higher DOPG (red correlation) content, the intensity fluctuations are slowed down indicated by an increase in the CRT $\tau_{80\% \text{ DOPG}} = 2.29 \pm 0.09 \text{ ms}$. The change in the bunching amplitudes $A_{dyn,0\% \text{ DOPG}}(t_g)$ and $A_{dyn,80\% \text{ DOPG}}(t_g)$ observed in the sg-FCS analysis (Fig. 6C) shows that the origin of the intensity fluctuations is not pp related but rather a dynamic process where the system switches between two FRET states on the 100 μs time scale (the acceptor signal upon direct acceptor excitation does not show any intensity fluctuations on this timescale, see *SI Appendix, section 10*). From these data, a two-FRET state model evolves in which, for both lipid compositions, the donor dye switches between a membrane bound and a membrane unbound state. Further analysis shows that the FRET efficiency of the membrane bound state is the same for both LUV compositions and that the low-FRET efficiency is slightly decreased further for the negatively charged LUVs (49). This is, however, not the only cause of the decreased average FRET value but sg-FCS also reveals a shift in the equilibrium constant for 80% DOPG content

($K_{0\% \text{ DOPG}} = 0.630 \pm 0.006$ and $K_{80\% \text{ DOPG}} = 0.246 \pm 0.002$), which indicates a longer dwell time in the low-FRET state compared to the high-FRET state. The resulting free energy diagram with the calculated dwell times is depicted in Fig. 6D. Overall, a model arises where the sensor works by both a decreased FRET efficiency of the low FRET state and a shift of the equilibrium towards the low FRET state when the LUVs are negatively charged (49).

Conclusion

Building on an extensive body of previous FCS and fluorescence lifetime work, we present here sg-FCS, an algorithm that combines correlation spectroscopy with fluorescence lifetime information to extract microscopy reaction rates and equilibrium constants. Without making any assumptions, the algorithm can easily be implemented when TCSPC data is available. sg-FCS directly reveals terms in the correlation function that are related to fluorescence lifetime changes and distinguishes them from photophysical processes. For two-state systems, analysis of the amplitudes as a function of the shrinking microtime threshold in sg-FCS makes it possible to extract the previously hidden equilibrium constants of the switching kinetics. Combining simulations and a robust model system based on a DNA origami pointer system, we prove the versatility by extracting equilibrium constants over a range of 2.5 orders of magnitude. Here, sg-FCS is applied to both immobilized structures and structures freely diffusing in solution.

In our experiments, we determine equilibrium constants from ~ 0.01 –10. The asymmetry with respect to $K = 1$ is related to the

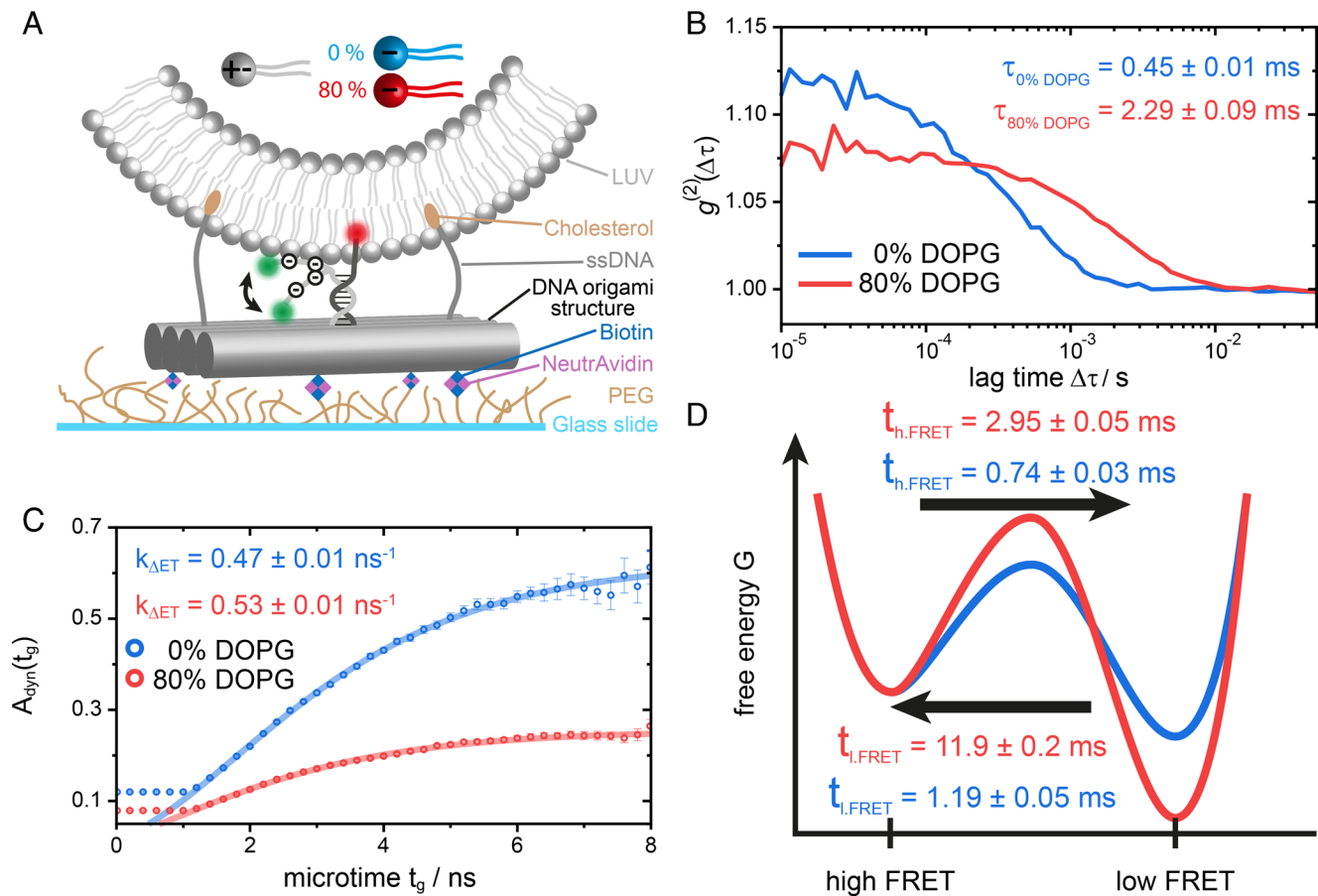


Fig. 6. Application of sg-FCS to a FRET-based membrane-voltage nanosensor. (A) Sketch of an immobilized charge-sensing DNA origami structure with a protruding donor acceptor dye pair attached to a LUV. (B) The $g^{(2)}(\Delta\tau, t_g = 0 \text{ ns})$ autocorrelation function of two representative donor trajectories for vesicles containing 0% DOPG/100% DOPC (blue) and 80% DOPG/20% DOPC (red). (C) The sg-FCS extracted bunching amplitudes $A_{\text{dyn},0\% \text{ DOPG}}(t_g)$ (blue circles) and $A_{\text{dyn},80\% \text{ DOPG}}(t_g)$ (red circles) as a function of gate width and fit to a two-state model (bold transparent line) to extract the equilibrium constant K and the quenching rate constant $k_{\Delta ET}$. (D) A free energy landscape describing the two states for the sensor with 0% (blue) and 80% DOPG LUVs (red).

reduced signal-to-noise ratio when the equilibrium is on the side of the high FRET states. In the future, a model that also incorporates a global fit to the acceptor correlation function could help to overcome this asymmetry and increase the dynamic range of the equilibrium constants. Interestingly, the distinction of photophysical on-off processes or diffusion, and biomolecular dynamics can even be achieved when both processes happen on similar time scales by using different subsets of photons for the correlation.

The fact that sg-FCS could directly reveal new insights for two projects of the laboratory, including a fluctuating tether on graphene and a new lipid-surface membrane-potential sensor, indicates the broad applicability of the method and suggests implementation of the method whenever TCSPC-data are available in combination with the autocorrelation analysis. Recent developments of commercial lifetime cameras suggest this approach can also be applied to widefield illumination where several molecules can be measured in parallel (52). In addition, smFRET experiments are now being performed in living cells (e.g., ref. 53) where sg-FCS promises to help extract quantitative dynamic information in more complex environments.

Materials and Methods

Simulations. We performed Monte Carlo simulations of a dynamic two-fluorescence-intensity-state system. The system switches stochastically between the two states $A \rightleftharpoons B$, where A denotes the fluorescence state and B the quenched

state. Simulations were performed with a self-written python script and detailed information on the rate constants and simulation length are described in *SI Appendix, section 1*.

Sample Preparation. The L-shaped DNA origami structures were prepared as described in ref. 38. After annealing, the DNA origami structures were gel purified with a 1% agarose gel to isolate correct-folded structures and to get rid of all excess staples. Details of the sequences of all DNA origami structures used are described in the *SI Appendix, section 5*. The same protocol was used for the FRET-based membrane charge sensor and is described in ref. 49. After purification, the origami structures were stored at -20°C until further use.

Single Molecule Surface Experiments. The DNA origami structures were immobilized in a LabTek-chamber by BSA-Biotin-NeutrAvidin chemistry. A concentration of 120 pM DNA origami structures was sufficient to find 20 to 30 single structures in a $10 \times 10 \mu\text{m}$ area without overlapping point spread functions. In order to reduce pp and photo bleaching, a reducing and oxidizing buffer system with $1 \times \text{TAE}$, 12.5 mM MgCl_2 , 2 mM Trolox (UV radiated until 13% of the Trolox was oxidized to Troloxquinone) and 1% (w/v) D-(+)-glucose was used in combination with an enzymatic oxygen scavenger system (250 U/mL glucose oxidase and 2,000 U/mL catalase). The LabTek chamber was sealed with Tough-Tag for 2 mL Eppis to hamper oxygen diffusion into the buffer. The LabTek chamber was placed on a home-built scanning confocal microscope. For fluorescent intensity trajectories, single DNA origami structures were picked from a $10 \times 10 \mu\text{m}$ area-scan. The single-molecule trajectories were acquired until one of the dyes bleached irreversibly. Detailed information of the setup as well as on the experimental parameters are provided in *SI Appendix, section 11*.

Single Molecule Solution Experiments. For solution experiments, the LabTek chamber was passivated with a 2 mg/mL BSA solution. The buffer system was identical as for the surface experiments with additionally 100 pM DNA origami concentration. Detailed information like the repetition rate, excitation intensity and data analysis are described in *SI Appendix, section 8*.

We provide all raw data used in this manuscript, as well as the python code for the analysis of the raw data on the zenodo.org platform: DOI:10.5281/zenodo.7254095 (54).

Data, Materials, and Software Availability. Raw TCSPC data (.ptu files) data have been deposited in zenodo.org (10.5281/zenodo.7254095) (54).

ACKNOWLEDGMENTS. P.T. and D.C.L. are grateful for support from the Deutsche Forschungsgemeinschaft (DFG, German Research Foundation) – Project-ID

201269156 – SFB 1032 Project A13 to PT and Project B3 to D.C.L.) and funding by the Bavarian Ministry of Science and the Arts through the ONE MUNICH Project “Munich Multiscale Biofabrication.” P.T. is indebted to the DFG for funding via grants nos. 470075523, 267681426, 459594986 and Germany's Excellence Strategy – EXC 2089/1-390776260. The authors thank Renuka Yaadav for rendering the DNA origami sketches.

Author affiliations: ^aDepartment of Chemistry and Center for NanoScience, Ludwig-Maximilians-Universität München, 81377 München, Germany

Author contributions: T.S., J.B., S.E.O., P.S., S.K., and P.T. designed research; T.S., S.E.O., P.S., and S.K. performed research; J.B. contributed new reagents/analytic tools; T.S. and S.E.O. analyzed data; D.C.L. improved FCS and smFRET experiments and analysis; and T.S., J.B., S.E.O., P.S., S.K., D.C.L., and P.T. wrote the paper.

1. M. Eigen, R. Rigler, Sorting single molecules: Application to diagnostics and evolutionary biotechnology. *Proc. Natl. Acad. Sci. U.S.A.* **91**, 5740–5747 (1994).
2. P. Schwille, F. J. Meyer-Almes, R. Rigler, Dual-color fluorescence cross-correlation spectroscopy for multicomponent diffusional analysis in solution. *Biophys. J.* **72**, 1878–1886 (1997).
3. L. Erokhova, A. Horner, P. Kügler, P. Pohl, Monitoring single-channel water permeability in polarized cells. *J. Biol. Chem.* **286**, 39926–39932 (2011).
4. D. Magde, E. Elson, W. W. Webb, Thermodynamic fluctuations in a reacting system—Measurement by fluorescence correlation spectroscopy. *Phys. Rev. Lett.* **29**, 705–708 (1972).
5. R. Rigler, J. Widengren, P. Kask, Fluorescence correlation spectroscopy with high count rate and low background: Analysis of translational diffusion. *Eur. Biophys. J.* **22**, 169–175 (1993).
6. C. B. Müller *et al.*, Precise measurement of diffusion by multi-color dual-focus fluorescence correlation spectroscopy. *Europhys. Lett.* **83**, 46001 (2008).
7. C. Eggeling *et al.*, Direct observation of the nanoscale dynamics of membrane lipids in a living cell. *Nature* **457**, 1159–1162 (2009).
8. M. H. Jensen, M. Sukumaran, C. M. Johnson, I. H. Greger, H. Neuweiler, Intrinsic motions in the N-terminal domain of an ionotropic glutamate receptor detected by fluorescence correlation spectroscopy. *J. Mol. Biol.* **414**, 96–105 (2011).
9. J. Kim, S. Doose, H. Neuweiler, M. Sauer, The initial step of DNA hairpin folding: A kinetic analysis using fluorescence correlation spectroscopy. *Nucleic Acids Res.* **34**, 2516–2527 (2006).
10. D. Nettels, A. Hoffmann, B. Schuler, Unfolded protein and peptide dynamics investigated with single-molecule FRET and correlation spectroscopy from picoseconds to seconds. *J. Phys. Chem. B* **112**, 6137–6146 (2008).
11. D. Magde, E. L. Elson, W. W. Webb, Fluorescence correlation spectroscopy. II. An experimental realization. *Biopolymers* **13**, 29–61 (1974).
12. S. Saffarian, I. E. Collier, B. L. Marmer, E. L. Elson, G. Goldberg, Interstitial collagenase is a Brownian ratchet driven by proteolysis of collagen. *Science* **306**, 108–111 (2004).
13. K. Chattopadhyay, S. Saffarian, E. L. Elson, C. Frieden, Measuring unfolding of proteins in the presence of denaturant using fluorescence correlation spectroscopy. *Biophys. J.* **88**, 1413–1422 (2005).
14. J. Widengren, U. Mets, R. Rigler, Fluorescence correlation spectroscopy of triplet states in solution: A theoretical and experimental study. *J. Phys. Chem.* **99**, 13368–13379 (1995).
15. J. Widengren, R. Rigler, U. Mets, Triplet-state monitoring by fluorescence correlation spectroscopy. *J. Fluoresc.* **4**, 255–258 (1994).
16. H. Sahoo, P. Schwille, FRET and FCS—friends or foes? *Chem. Phys. Chem.* **12**, 532–541 (2011).
17. T. Torres, M. Levitus, Measuring conformational dynamics: A new FCS-FRET approach. *J. Phys. Chem. B* **111**, 7392–7400 (2007).
18. J. Enderlein, I. Gregor, Using fluorescence lifetime for discriminating detector afterpulsing in fluorescence-correlation spectroscopy. *Rev. Sci. Instrum.* **76**, 33102 (2005).
19. A. Ghosh *et al.*, Quantifying microsecond transition times using fluorescence lifetime correlation spectroscopy. *J. Phys. Chem. Lett.* **8**, 6022–6028 (2017).
20. D. C. Lamb, A. Schenk, C. Röcker, C. Scalfi-Happ, G. U. Nienhaus, Sensitivity enhancement in fluorescence correlation spectroscopy of multiple species using time-gated detection. *Biophys. J.* **79**, 1129–1138 (2000).
21. T. A. Laurence *et al.*, Correlation spectroscopy of minor fluorescent species: Signal purification and distribution analysis. *Biophys. J.* **92**, 2184–2198 (2007).
22. C. Eggeling, J. R. Fries, L. Brand, R. Günther, C. A. Seidel, Monitoring conformational dynamics of a single molecule by selective fluorescence spectroscopy. *Proc. Natl. Acad. Sci. U.S.A.* **95**, 1556–1561 (1998).
23. A. Barth *et al.*, Dynamic interactions of type I cohesin modules fine-tune the structure of the cellulosome of *Clostridium thermocellum*. *Proc. Natl. Acad. Sci. U.S.A.* **115**, E11274–E11283 (2018).
24. H. Sanabria *et al.*, Resolving dynamics and function of transient states in single enzyme molecules. *Nat. Commun.* **11**, 1231 (2020).
25. K. Gurusathan, M. Levitus, FRET fluctuation spectroscopy of diffusing biopolymers: Contributions of conformational dynamics and translational diffusion. *J. Phys. Chem. B* **114**, 980–986 (2010).
26. D. C. Lamb, A. Schenk, C. Röcker, G. U. Nienhaus, Determining chemical rate coefficients using time-gated fluorescence correlation spectroscopy. *J. Phys. Org. Chem.* **13**, 654–658 (2000).
27. G. Bonnet, O. Krichesky, A. Libchaber, Kinetics of conformational fluctuations in DNA hairpin-loops. *Proc. Natl. Acad. Sci. U.S.A.* **95**, 8602–8606 (1998).
28. S. Doose, H. Neuweiler, M. Sauer, Fluorescence quenching by photoinduced electron transfer: A reporter for conformational dynamics of macromolecules. *Chemphyschem* **10**, 1389–1398 (2009).
29. S. Doose, H. Neuweiler, M. Sauer, A close look at fluorescence quenching of organic dyes by tryptophan. *Chemphyschem* **6**, 2277–2285 (2005).
30. B. Lounis, W. E. Moerner, Single photons on demand from a single molecule at room temperature. *Nature* **407**, 491–493 (2000).
31. P. Tinnefeld *et al.*, Antibunching in the emission of a single tetrachromophoric dendritic system. *J. Am. Chem. Soc.* **124**, 14310–14311 (2002).
32. M. Orrit *et al.*, Single molecule fluorescence: From excitation spectra to time correlation. *J. Lumin.* **60–61**, 991–996 (1994).
33. P. Tinnefeld, D.-P. Herten, M. Sauer, Photophysical dynamics of single molecules studied by spectrally-resolved fluorescence lifetime imaging microscopy (SFLIM). *J. Phys. Chem. A* **105**, 7989–8003 (2001).
34. J. Vogelsang *et al.*, A reducing and oxidizing system minimizes photobleaching and blinking of fluorescent dyes. *Angew. Chem. Int. Ed. Engl.* **47**, 5465–5469 (2008).
35. J. Vogelsang, T. Cordes, C. Forthmann, C. Steinhauer, P. Tinnefeld, Controlling the fluorescence of ordinary oxazine dyes for single-molecule switching and superresolution microscopy. *Proc. Natl. Acad. Sci. U.S.A.* **106**, 8107–8112 (2009).
36. T. Cordes, J. Vogelsang, P. Tinnefeld, On the mechanism of trolox as antiblinking and antibleaching reagent. *J. Am. Chem. Soc.* **131**, 5018–5019 (2009).
37. J. Stein *et al.*, Toward Absolute Molecular Numbers in DNA-PAINT. *Nano Lett.* **19**, 8182–8190 (2019).
38. I. Kamińska *et al.*, Graphene energy transfer for single-molecule biophysics, biosensing, and super-resolution microscopy. *Adv. Mater.* **33**, e2101099 (2021), 10.1002/adma.202101099, 2101099.
39. M. Götz *et al.*, A blind benchmark of analysis tools to infer kinetic rate constants from single-molecule FRET trajectories. *Nat. Commun.* **13**, 5402 (2022).
40. I. Kamińska *et al.*, Distance dependence of single-molecule energy transfer to graphene measured with DNA origami nanopositioners. *Nano Lett.* **19**, 4257–4262 (2019).
41. A. Zumbusch, L. Fleury, R. Brown, J. Bernard, M. Orrit, Probing individual two-level systems in a polymer by correlation of single molecule fluorescence. *Phys. Rev. Lett.* **70**, 3584–3587 (1993).
42. J. Yu, R. Lammi, A. J. Gesquiere, P. F. Barbara, Singlet-triplet and triplet-triplet interactions in conjugated polymer single molecules. *J. Phys. Chem. B* **109**, 10025–10034 (2005).
43. S. T. Hess, W. W. Webb, Focal volume optics and experimental artifacts in confocal fluorescence correlation spectroscopy. *Biophys. J.* **83**, 2300–2317 (2002).
44. D. E. Koppel, Statistical accuracy in fluorescence correlation spectroscopy. *Phys. Rev. A* **10**, 1938–1945 (1974).
45. S. Krause *et al.*, Graphene-on-glass preparation and cleaning methods characterized by single-molecule DNA origami fluorescent probes and Raman spectroscopy. *ACS nano* **15**, 6430–6438 (2021).
46. L. A. Masullo *et al.*, Pulsed interleaved MINIFLUX. *Nano Lett.* **21**, 840–846 (2021).
47. S. A. McKinney, C. Joo, T. Ha, Analysis of single-molecule FRET trajectories using hidden Markov modeling. *Biophys. J.* **91**, 1941–1951 (2006).
48. P. C. Nickels *et al.*, Molecular force spectroscopy with a DNA origami-based nanoscopic force clamp. *Science* **354**, 305–307 (2016).
49. S. E. Ochmann, T. Schröder, C. M. Schulz, P. Tinnefeld, Quantitative single-molecule measurements of membrane charges with DNA origami sensors. *Anal. Chem.* **94**, 2633–2640 (2022).
50. J. I. Elliott *et al.*, Membrane phosphatidyserine distribution as a non-apoptotic signalling mechanism in lymphocytes. *Nat. Cell Biol.* **7**, 808–816 (2005).
51. N. M. Rysavy *et al.*, Beyond apoptosis: The mechanism and function of phosphatidyserine asymmetry in the membrane of activating mast cells. *Bioarchitecture* **4**, 127–137 (2014).
52. N. Oleksievets *et al.*, Single-molecule fluorescence lifetime imaging using wide-field and confocal-laser scanning microscopy: A comparative analysis. *Nano Lett.* **22**, 6454–6461 (2022).
53. W. B. Asher *et al.*, Single-molecule FRET imaging of GPCR dimers in living cells. *Nat. Methods* **18**, 397–405 (2021).
54. T. Schröder *et al.*, Datafor “Shrinking gate fluorescence correlation spectroscopy yieldsequilibrium constants and separates photophysics from structural dynamics”, Zenodo. <https://zenodo.org/record/7254095>. Deposited 26 October 2022.